Check for updates

View Article Online
View Journal

NJC
New Journal of Chemistry
A journal for new directions in chemistry
Accepted Manuscript

This article can be cited before page numbers have been issued, to do this please use: Q. Yang, S. Wei, L. Zhang and R. Yang, *New J. Chem.*, 2020, DOI: 10.1039/D0NJ03375H.

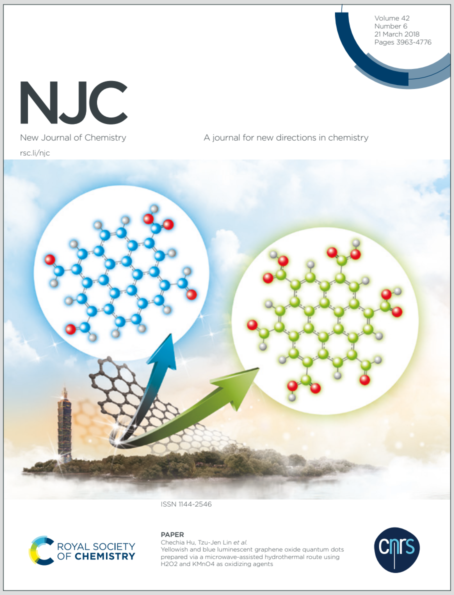

Volume 42
Number 6
21 March 2018
Pages 3963-4776

NJC
New Journal of Chemistry
A journal for new directions in chemistry
rsc.li/njc

ISSN 1144-2546

ROYAL SOCIETY OF CHEMISTRY

PAPER
Chechia Hu, Tzu-Jen Lin *et al.*
Yellowish and blue luminescent graphene oxide quantum dots prepared via a microwave-assisted hydrothermal route using H2O2 and KMnO4 as oxidizing agents

cnrs

This is an Accepted Manuscript, which has been through the Royal Society of Chemistry peer review process and has been accepted for publication.

Accepted Manuscripts are published online shortly after acceptance, before technical editing, formatting and proof reading. Using this free service, authors can make their results available to the community, in citable form, before we publish the edited article. We will replace this Accepted Manuscript with the edited and formatted Advance Article as soon as it is available.

You can find more information about Accepted Manuscripts in the Information for Authors.

Please note that technical editing may introduce minor changes to the text and/or graphics, which may alter content. The journal's standard Terms & Conditions and the Ethical guidelines still apply. In no event shall the Royal Society of Chemistry be held responsible for any errors or omissions in this Accepted Manuscript or any consequences arising from the use of any information it contains.

ROYAL SOCIETY OF CHEMISTRY

rsc.li/njc

View Article Online
DOI: 10.1039/D0NJ03375H

Ultrasound assisted synthesis of $BiVO_4$/C-Dots/g-C_3N_4 Z-scheme heterojunction photocatalyst for degradation of minocycline hydrochloride and Rhodamine B: Optimization and mechanism investigation

Qiang Yang[1], Siqi Wei[1], Limei Zhang[1], and Rui Yang[1,*]

Abstract

As solid-state electron medium of the composite photocatalyst, Carbon dots (C-dots) possess the property of increasing the transition process of photogenerated carriers and inhibit their rapid recombination. In this work, a novel and efficient Z-scheme heterojunction $BiVO_4$/C-dots/g-C_3N_4 photocatalyst with C-Dots as the photoelectron transfer center has been designed. FTIR, HRTEM, TEM, XRD and PL were used to investigate the physical and chemical properties of the photocatalysts. Due of the up-conversion photoluminescence characteristics of carbon dots, the $BiVO_4$/C-dots/g-C_3N_4 photocatalyst exhibits a significant interfacial charge transfer capability and a broader visible absorption range. In addition, the photocatalytic activity of the photocatalysts was improved by changing the doping amount and optimizing the synthesis conditions. As a result, $BiVO_4$/C-dots/g-C_3N_4 composites showed remarkable degradation efficiency of minocycline hydrochloride (Mino-HCl) and Rhodamine B (RhB) under a near-visible LED light. Furthermore, the photodegradation efficiency of $BiVO_4$/C-dots/g-C_3N_4-40 photocatalyst was conspicuously improved than that of pure $BiVO_4$, g-C_3N_4 and other content ratio composites. The comparative experiment also proves that the introduction of carbon dots can enhance the performance of photocatalyst. Finally, the possible catalytic mechanism was explored via free radical capture experiment for active substances, and the excellent photostability and reusability of $BiVO_4$/C-dots/g-C_3N_4 composites were proved through three cycle of experiments.

Keywords Z-scheme heterojunction, photocatalysis, g-C_3N_4, carbon dots, electron medium

1. Introduction

Over recent years, improper treatments of industrial, medical and other types of wastewater have caused serious water pollution, such as organic pollutants and antibiotic wastewater[1, 2].These pollutants severely threaten the ecological environment of the natural water as well as human health. For example, an emerging broad-spectrum antibiotic, minocycline hydrochloride (Mino-HCl), due to it cannot be completely absorbed by organisms, and its metabolites may be discharged into the environment in their original state, resulting in antibiotic wastewater pollution[3]. In addition, as an important chemical product, dye has great economic value, but its wastewater is highly toxic, carcinogenic, difficult to degrade and easy to cause serious water pollution[4]. To solve this environmental problem, researchers have focused on the development of novel photocatalysts. In recent years, many environmentally friendly photocatalysts have been developed and applied to the production of clean fuels and environmental restoration[5-8]. Using solar energy and reusable semiconductor materials to photodegrade pollutants is a promising method of environmental remediation[9, 10].

Graphite-phase carbon nitride (g-C_3N_4) has caught widespread attentions of researchers because of its narrow band gap and suitable conduction band position[11-14], and the irradiation of visible light can stimulate g-C_3N_4 to generate photoelectrons and oxidize O_2 to form superoxide radicals ($\cdot O_2^-$) [15, 16]. However, the weak interaction (van der Waals force) among adjacent

[1] *School of Chemistry and Chemical Engineering, Southwest University, No.2 Tiansheng Road, Chongqing 400715, People's Republic of China*

**Corresponding author. E-mail address: ruiyang@swu.edu.cn*

View Article Online
DOI: 10.1039/D0NJ03375H

C-N layers in g-C_3N_4 will inhibit the separation of photogenerated carrier[17]. Accordingly, a lot of efforts has been put into improving the photocatalytic performance of g-C_3N_4, such as the construction of nanostructures[18] and coupling with metal[19] and nonmetallic semiconductors[20]. Carbon dots (C-dots) as a novel nanomaterials, has unique photogenerated electron transfer and up-conversion photoluminescence (PL) properties [21], which makes the carbon dots modified g-C_3N_4 has a good degradation effect on photocatalytic dyes and phenols[22-24]. Besides, the conjugated π structure of C-Dots can interact C-Dots with semiconductor to establish stable composite materials[25]. In recent years, many composite catalysts synthesized by doping carbon dots have been reported to degrade wastewater[26, 27].

Bismuth vanadate ($BiVO_4$) is a green, non-toxic semiconductor photocatalyst, which has been widely studied due to its narrow band gap and responses under visible light [28]. $BiVO_4$ generally has three crystal form, namely orthogonal crystal, tetragonal zircon and monocline scheelite type, respectively[29, 30]. The photocatalytic activity of monoclinic scheelite $BiVO_4$ is higher than that of other crystal forms, because its degree of distortion around Bi^{3+} and V^{5+} is very high, which increases the degree of local polarization and is conducive to separate the photogenerated electrons and holes. However, pure $BiVO_4$ still has a low utilization rate of visible light and a high photogenerated carrier binding rate after hybrid with different semiconductor materials, such as $BiVO_4/Bi_2O_3$ [29]and $WO_3/BiVO_4$ [31]. To settle these problems, a novel Z-scheme heterojunction photocatalyst was constructed by combining $BiVO_4$ and C-Dots with g-C_3N_4. Notably, these $BiVO_4$/C-Dots/g-C_3N_4 composites can not only retain the reduction capacity of g-C_3N_4 at the negative CB position, but also improve the oxidation capacity of $BiVO_4$ at the positive VB position. Moreover, Z-scheme heterojunction photocatalyst can also improve the photocatalytic activity owing to its excellent separation efficiency of photogenerated electrons-holes and a wide absorption spectrum. To our knowledge, there is currently no research on constructing Z-scheme $BiVO_4$/C-Dots/g-C_3N_4 heterojunction photocatalysts using C-dots as an electron-hole bridge and research on its degradation efficiency of minocycline hydrochloride.

Herein, a novel Z-scheme $BiVO_4$/C-Dots/g-C_3N_4 heterojunction photocatalyst was fabricated by sonication. The $BiVO_4$/C-Dots/g-C_3N_4 photocatalysts showed obvious photoactivity to degrade Rhodamine B (RhB) and minocycline hydrochloride (Mino-HCl) under LED light irradiation, and after introducing C-Dots, the photocatalytic performance was significantly improved compared with that of the binary catalyst. Simultaneously, the impacts of different conditions on the photocatalytic properties of the composites were investigated through comparative experiments. The stability of photocatalyst was evaluated by three cyclic tests. And the degradation mechanism of contaminants by $BiVO_4$/C-Dots/g-C_3N_4 was investigated by free radical capture experiment.

2. Experimental

2.1. Materials and reagents

Ammonium metavanadate (NH_4VO_3), ammonia ($NH_3\cdot H_2O$), Bismuth nitrate ($Bi(NO_3)_3\cdot 5H_2O$), melamine ($C_3N_3(NH_2)_3$), nitric acid (HNO_3),acetic acid (CH_3COOH), citric acid (CA), formamide (CH_3NO), EDTA-2Na, 4-benzoquinone (BQ), isopropanol (IPA), rhodamine B and minocycline hydrochloride were obtained from the Shanghai Macklin Biochemical Co., LTD, Shanghai, China.

2.2. Preparation

2.2.1 Synthesis of C-dots

The C-Dots were obtained by a hydrothermal method in previous work[32]. Firstly, 1 g of citric acid and 10 mL formamide were mixed and stirred, then transferred to the autoclave reactor and heated for 4 h at 180 °C. The solution was centrifuged (8000 rpm, 10min) 3 times to remove insoluble particles. Subsequently, the precipitation was collected by adding huge amount of acetone (eluent) into the solution, then centrifuged and dried it. At last, the C-Dots powders were prepared into solutions with concentrations of 0.2, 0.5, 1, 2, 5, 10 and 20 mg/mL, respectively.

View Article Online
DOI: 10.1039/D0NJ03375H

2.2.2 Preparation of g-C_3N_4/C-Dots and $BiVO_4$

g-C_3N_4/C-Dots was prepared by adding C-Dots to the melamine and calcining. Briefly, melamine (2 g) and C-Dots solution (2 mL) were dispersed in DI water (10 mL), and the precipitation was dried at 80 ℃ for 1 h. The resulting powder was calcined in a muffle furnace at 550℃ for 4 h (the heating rate was 5 ℃/min). Finally, the light-yellow solid was ground into fine powder, which was named GCDs. Pure g-C_3N_4 (GCN) was synthesized through direct calcination of melamine without C-Dots, and the procedures as same as described above.

$BiVO_4$ was prepared through a hydrothermal route. Firstly, 5 mmol $Bi(NO_3)_3 \cdot 5H_2O$ was dissolved in 10 mL acetic acid to form solution A, and 5 mmol NH_4VO_3 was added into 50 mL deionized water to form solution B. Then the solution B was dropped into solution A, and ultrasonic treatment for 30 min to form yellow precipitation. Subsequently, the pH of the suspension was adjusted to 9 with $NH_3 \bullet H_2O$. After stirring for 2 h, the solution was heated at 140℃ for 20 hours in autoclave. After the reaction, it was cooled to ambient temperature, centrifuged, washed and dried at 80 ℃ overnight and the obtained powder was calcined at 450° for 2h.

2.2.3 Synthesis of $BiVO_4$/C-Dots/g-C_3N_4

$BiVO_4$/C-Dots/g-C_3N_4 (BCG) was construct through ultrasonic treatment and calcination. 1 g of above GCDs was mixed with a certain amount of $BiVO_4$, and transferred into 50 mL deionized water to form a suspension. After ultrasonic treatment for 30 min, the suspension continued stirring for 10 h. The resulting powder was washed several times and dried overnight in a vacuum drying oven, then heated to 450℃ for 2 h (5 ℃/min). Following the above procedure, BCG composites with different mass ratios were synthesis by adding 20, 30, 40, 50 % $BiVO_4$ (labeled as BCG-20, BCG-30, BCG-40, BCG-50, respectively).

2.3. Characteristics

A transmission electron microscope (TEM) and high resolution TEM (HRTEM) date was obtained with on the JEM-2100. X-ray diffraction (XRD, SHIMADZU 7000) was used to characterize the crystalline structure of all the prepared photocatalysts. X-ray photoelectron spectroscopy (XPS, Perkin-Elmer PHI 5000) was used to measure the chemical state of element and element composition. UV–vis absorption spectra were measured on a Shimadzu UV-2700 spectrometer, and the Fourier transform infrared (FT-IR, FTIR-8400S) spectra were also recorded. PL spectra dates were obtained on F-7000 spectrophotometer (Hitachi, Japan). The electron spin resonance (ESR) was measured on a Bruker model ESR ELEXSYS II spectrometer. Specific surface areas and pore structures are probed by measuring volumetric N_2 adsorption-desorption isotherms at liquid nitrogen temperature, using an ASAP 2460 instrument (Micromeritics, USA). Raman spectra were also recorded on HORIBA LarRAM HR 800.

2.4. Photoelectrochemical analysis

The photoelectric current (PC) and electrochemical impedance spectroscopy (EIS) of the photocatalyst were recorded through a CHI660E electrochemical workstation using a standard three-electrode system with a working electrode, a Pt wire counter electrode and an Ag/AgCl reference electrode. The preparation method of electrodes would be presented in detail as follow: 5 mg of samples was added into the mixed solution of 0.5 mL of deionized water, 0.5 mL of alcohol and 50 μL of Nafion and then uniformly dispersed by ultrasound to obtain a suspension. Then, 2 μL of suspension was spread onto a 1 cm^2 ITO glass and dried under ambient condition. A 300W LED was used as the visible light source. And a 0.5 M Na_2SO_4 aqueous solution was used as the electrolyte.

2.5. Photocatalytic activity and photostability

The photocatalytic performance of all the photocatalyst was investigated by degradation of Rhodamine B (RhB, 20 mg/L) and minocycline hydrochloride (Mino-HCl, 20 mg/L) under the 350W LED (460 nm), and the simple photocatalytic device is shown in Fig. S1. Briefly, 50 mg of the prepared photocatalyst was dispersed into 50 mL of 20 mg/L RhB (Mino-HCl) solution, stirred in the dark and kept for 30 minutes before irradiation to reach the adsorption-desorption equilibrium. The suspension samples (3 mL) were collected and filtered to remove photocatalyst, and using the UV-vis absorption spectrophotometer to measure the concentration of the solution. The stability of BCG composites was evaluated by three cyclic tests.

3. Result and discussion

3.1. Characterization of the photocatalyst

3.1.1. XRD analysis

In order to investigate the crystal lattice structure, the XRD analysis of different photocatalysts as shown in Fig. 1. According to the reported[33], the XRD pattern of GCN exhibit primary diffraction peak near 27.5° corresponds to the (002) planes [34, 35]. Pure GCN and GCDs show similar and obviously peaks at 27.5°, probably because the concentration of C-Dots is limited, the crystallinity is low, and the dispersion is high. The pure $BiVO_4$ has obvious diffraction peaks at 2θ =18.7°, 19.0°, 28.9°, 30.5°, 34.6°, 35.2°, 39.9°, 42.5°, 46.8°, 47.3°, 53.3°, 58.4° and 59.3° are ascribed to the crystal planes of monoclinic $BiVO_4$, which is (110), (011), (121), (040), (200), (002), (211), (150), (060), (240), (161), (321) and (123), respectively[36, 37]. Moreover, there were no other characteristic peaks, indicating that the synthesized $BiVO_4$ had high purity and single crystal type. Fig. 1d-g demonstrate the XRD analysis of BCG photocatalyst with different $BiVO_4$ amount. The peak of 2θ = 27.5 ° in BCG-20 is ascribed to the (002) crystal plane of GCN, which indicates that $BiVO_4$ successfully binds to GCDs. As the $BiVO_4$ content increases, the diffraction peaks intensity of $BiVO_4$ increase, while the peaks intensity of GCDs decrease. The results show that we successfully prepared BCG composites.

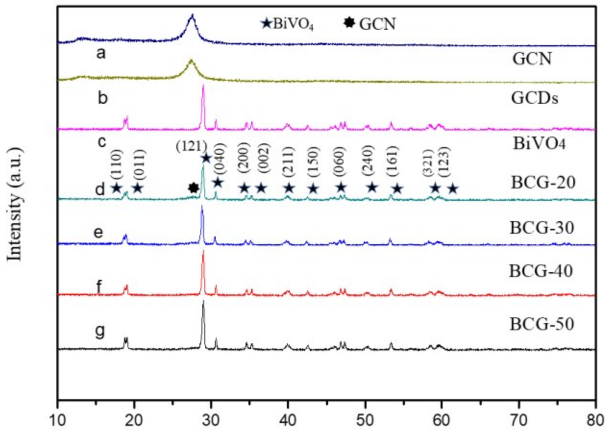

Fig. 1. XRD patterns of (a) GCN, (b) GCDs, (c) $BiVO_4$, (d) BCG-20, (e) BCG-30, (f) BCG-40, and (g) BCG-50.

3.1.2. Morphology of catalysts

The morphology and microstructure of the prepared photocatalyst were characterized by transmission electron microscopy and high-resolution transmission

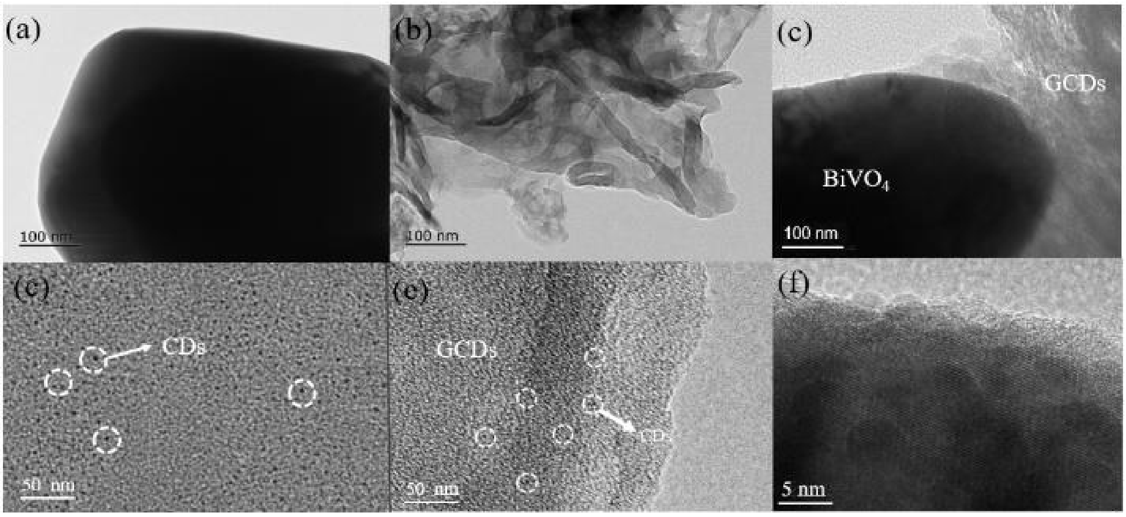

Fig. 2. TEM images of (a) $BiVO_4$, (b) GCN, (c) BCG-40, and HRTEM images of (d) C-Dots, (e) GCDs and (f) BCG-40.

View Article Online
DOI: 10.1039/D0NJ03375H

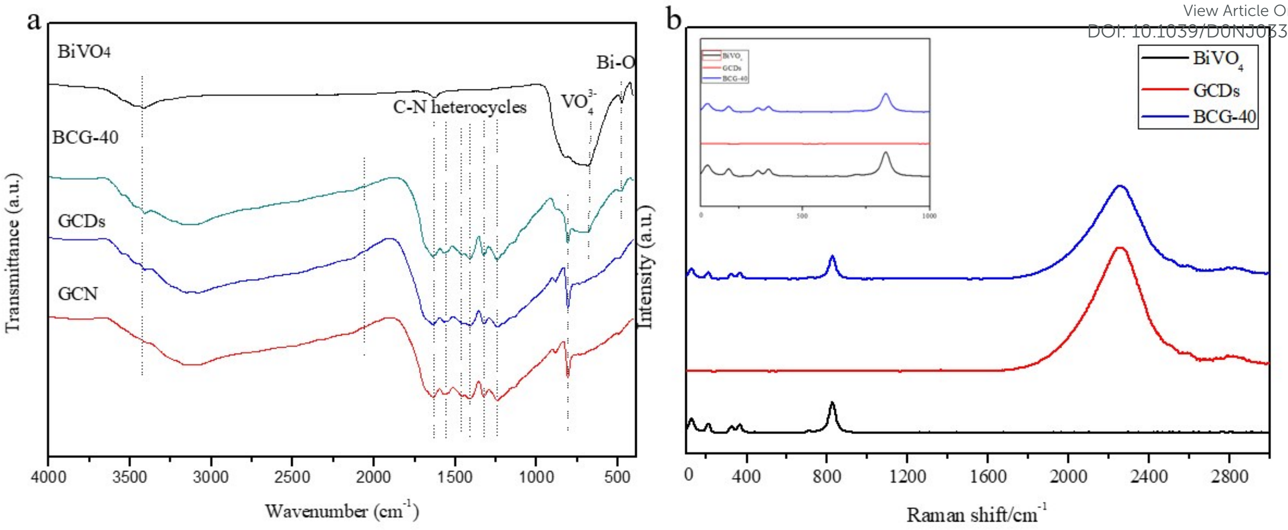

Fig. 3. (a) FT-IR spectra and (b) Raman spectra of as-prepared photocatalysts.

electron microscopy, and the results are shown in Fig. 2. From the Fig. 2a, it can be observed that the pristine $BiVO_4$ exhibit clearly regular crystals. Fig. 2b exhibits the TEM image of pure GCN， which can clearly see the irregular layered sheet structure. Fig. 2d and 2e show HRTEM images of C-Dots solution and GCDs, and it can be clearly seen that the C-Dots adhere uniformly on the surface of GCN. Fig. 2c and Fig. 2f are the TEM and HRTEM images of BCG-40. It can be obviously observed $BiVO_4$ coat on the surface of GCDs, and the binding of carbon points and nanoparticles can also be observed between the interfaces of the two.

3.1.3. FT-IR and Raman analysis

The FT-IR spectra of as-prepared composites are showed in Fig. 3a, which was used to investigate the chemical function groups of it. For the $BiVO_4$, the peak at 731 cm^{-1}, 517 cm^{-1} and 475 cm^{-1} are deem to be the VO_4^{3-}, Bi-O and V-O characteristic peak of $BiVO_4$, respectively[38, 39]. While the peak at 1619 cm^{-1} and 3415 cm^{-1} correspond to bending and stretching vibrations in H_2O molecules. The characteristic peak of pure GCN at 808 cm^{-1} is the typical stretching vibration peak of the 3-s-triazine ring units in GCN [40], and the peaks between 1200-1700 cm^{-1} was associated with two vibration modes C=N and C-N, which is a unique skeleton vibration of the aromatic ring[41]. Among them, the several weak peaks at 1240 cm^{-1}, 1322 cm^{-1}, and 1410 cm^{-1} are attracted by the C-N stretching vibration of sp^3 hybrid, the 1638 cm^{-1} is caused by the C=N stretching vibration of sp^2 hybrid. The broad band ranged from 3080-3300 cm^{-1} is usually attributed to the N-H stretching vibration of GCN, which is caused by the occurrence of several hydrogenated nitrogen atoms on the prepared GCN nanosheets, and the N-H stretching vibration at the defect of the aromatic ring. For BCG-40 composites, the main peaks of GCN and $BiVO_4$ still existed which indicated that the combination of $BiVO_4$ does not affect the structure of the GCDs. Although the characteristic peaks of $BiVO_4$ are weak, it can still prove that $BiVO_4$ successfully incorporated into GCDs and prepared BCG. Raman spectral analysis was performed on samples $BiVO_4$ and GCDs, and the results were shown in Fig. 3b. The vibrational bands of pure $BiVO_4$ at approximate 121 cm^{-1}, 210 cm^{-1}, 323 cm^{-1}, 829 cm^{-1} are measured, which are consistent with the previous report[38, 42, 43]. The typical D and G peaks in Raman spectrum are not observed in the figure, which may be due to the fluorescence effect of GCDs itself, which produces a strong background value under the action of excitation light[44]. However, it can be seen that the characteristic peak at 2200 cm^{-1} may be due to a small amount of C≡N bonds produced by high temperature processing.

View Article Online
DOI: 10.1039/D0NJ03375H

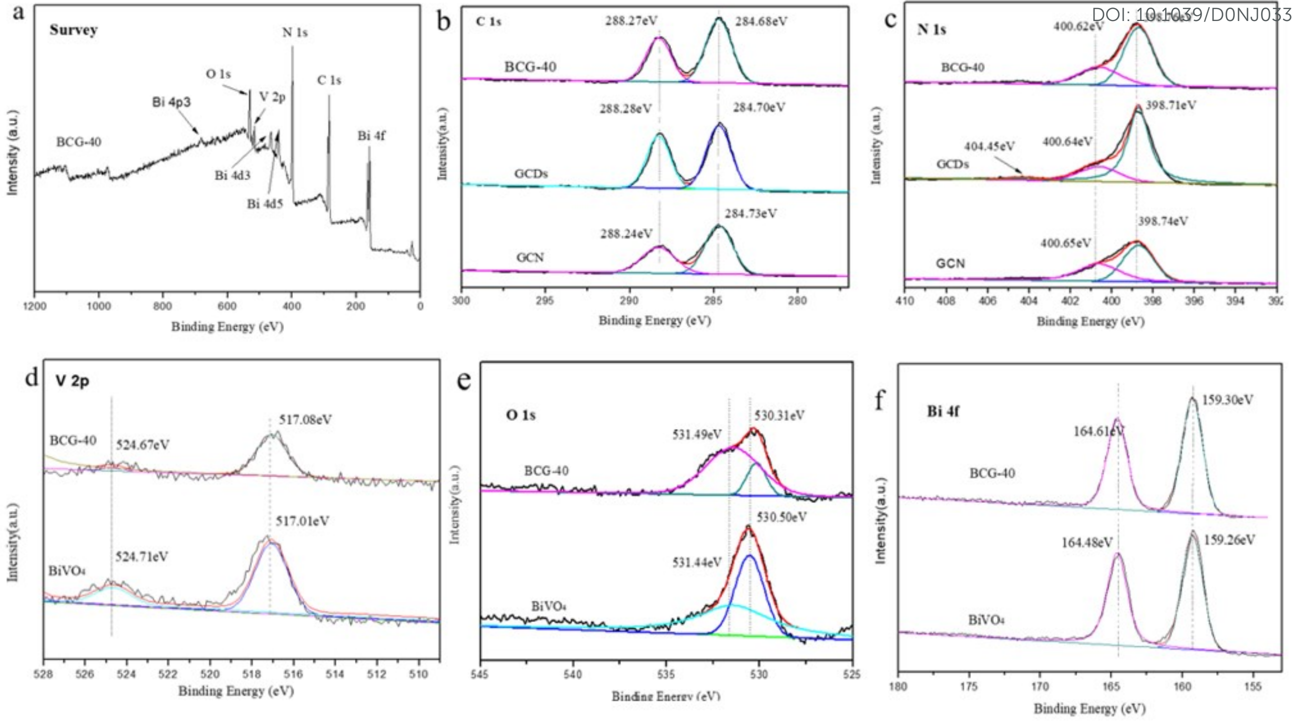

Fig. 4. XPS analysis of as-prepared photocatalysts: (a) survey spectrum (b) C*1s*, (c) N*1s*, (d) V*2p*, (e) O *1s*, and (f) Bi*4f.*

3.1.4 XPS analysis

XPS analysis was performed to investigate the elemental composition and the chemical states of the as-prepared catalysts. Shown in Fig. 4a, the survey XPS spectrum shows that Bi, O, V, N, and C elements exist in BCG-40 composite, as well as the characteristic peaks generated by Bi*4f*, O*1s*, V*2p*, N*1s*, C*1s*. For the pure GCN in the Fig. 4b, the peaks of C*1s* around 284.73 and 288.24 eV can be assigned to the C-C and C-$(N)_3$[45, 46]. And Fig. 4c shows that N*1s* spectrum features with three peaks at 398.71 eV, 400.64 eV, 404.45 eV[14]. The peak at 398.71 eV can be assigned to the C=N-C functional group formed by the hybridization of the sp^2 orbital of N atom and two C atoms. While the peak at 400.64 eV can be attributed to the N-$(C)_3$ group and the weak peak at 404.45 eV is the characteristic peak of graphitized species[47, 48]. Compared with pure GCN and GCDs, the disappearance of BCG-40 composites peak at 404.45 eV proves that $BiVO_4$ covers the graphitic species, and π-electrons from CN heterocycles used to couple with GCDs through an attractive force instead of binding with C and N atoms in GCDs[49]. For $BiVO_4$ in Fig. 4d, the characteristic peaks of V*2p* in XPS spectrum at 517.08 eV and 524.71 eV, corresponding to $V2p_{3/2}$ and $V2p_{1/2}$ in V-O, respectively, which is consistent with the binding energy of V^{5+} in crystal structure[50]. Fig. 4e shows the XPS spectra of O*1s*. The O*1s* peak can be split into two peaks at 530.50 and 531.44 eV, meaning the presence of two forms of oxygen on surface of the samples, which are attributed to Bi-O in $BiVO_4$ and H_2O, respectively[26, 51]. In the XPS spectra of Bi*4f* (Fig. 4f), the peaks are mainly concentered at 159.26 and 164.48 eV, which are attributed to the characteristic peaks of $Bi4f_{5/2}$ and $Bi4f_{7/2}$ binding energies ,respectively[52]. It is demonstrated that the Bi element of $BiVO_4$ is Bi^{3+}. Finally, the FT-IR and XPS analysis proved that the synthesis of BCG composites is successful.

3.1.5. PL analysis

Photoluminescence emission primarily comes from the recombination of photogenerated electrons and holes in semiconductors, and its spectrum can indicate the recombination rate of photo-excited electrons and holes, the low emission peak intensity represents the low recombination rate [53]. Fig. 5 shows the steady-state fluorescence spectra of pure GCN, GCN/$BiVO_4$, GCDs, BCG-40 and pure $BiVO_4$ under 380 nm excitation. It can be clearly observed that the pure GCN has a strong

View Article Online
DOI: 10.1039/D0NJ03575H

emission peak near 470 nm, which coincides with the visible light absorption band of the GCN photocatalyst[53]. The PL spectra shows that the photoluminescence intensity of GCN, GCDs and BCG-40 decreases in turn and the relative photoluminescence intensity of $BiVO_4$ is too low to be detected. Among these, pure GCN has the highest emission peak intensity, which means that the charge recombination rate of GCN is high, resulting in poor photocatalytic efficiency. The BCG-40 composite has the lowest emission peak intensity, which represents the best photocatalytic activity. Moreover, the photoluminescence intensity of BCG-40 is lower than that of GCN/$BiVO_4$, which further proves that the carbon dot as an electron transfer center enhances the separation of photogenerated carriers. These PL results of the prepared catalyst are also consistent with the photocatalytic activity of contaminant degradation, which will be confirmed in the following photocatalytic activity tests.

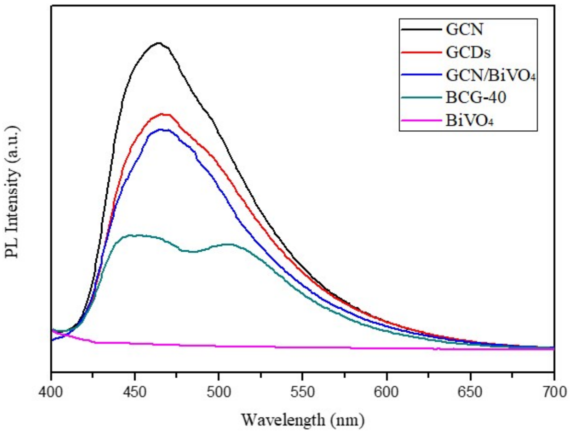

Fig. 5. PL spectra of as-prepared GCN, GCDs, GCN/$BiVO_4$, BCG-40 and $BiVO_4$.

3.1.6. Photocurrent response and EIS analysis

A high charge separation rate and quick migration of photoinduced charges are two key factors for increasing the photoactivity of a photocatalyst[54], in order to demonstrate the separation and transfer feature of the photogenerated electron-hole pairs, the photocurrent response (PC) tests and the electrochemical impedance spectroscopy (EIS) of as-prepared $BiVO_4$, GCN, GCDs and BCG-40 were measured. As shown in Fig. 6a, pure $BiVO_4$ and GCN have weak photocurrent intensity because of the low separation efficiency of the photogenerated carriers. However, the photocurrent intensity of GCDs was higher as compared with that of $BiVO_4$ and GCN, and BCG-40 exhibits the highest photocurrent intensity, implying that the introduction of C-Dots can help to accelerate the transfer and separation of photogenerated electron-holes. Moreover, to further investigate the charge transfer resistance and separation efficiency of the carriers, EIS measurement of as-prepared photocatalysts were also carried out and displayed in Fig. 6b. The diameter of the semicircle of the EIS Nyquist plots is related to the transfer efficiency of

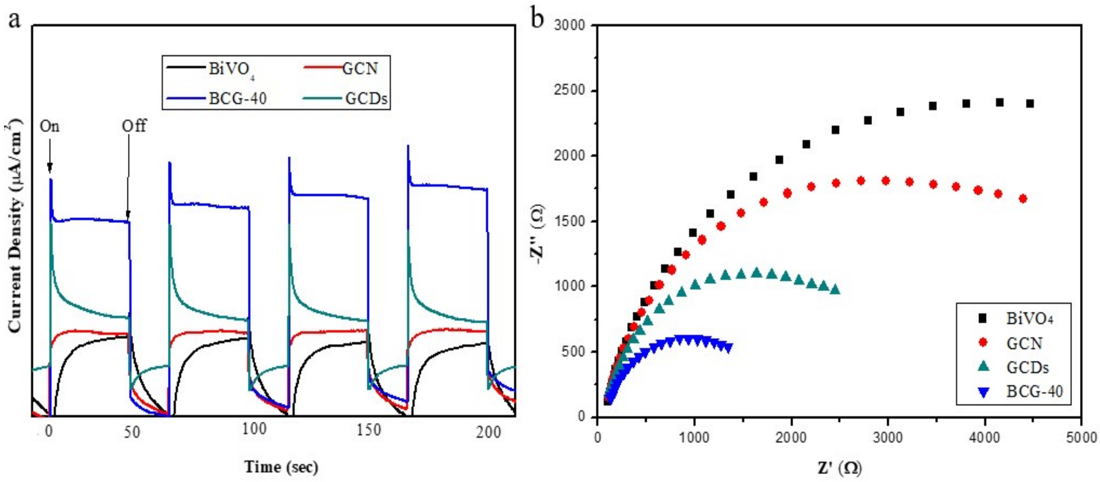

Fig. 6. (a) Photocurrent response and (b) EIS Nyquist plot of the pure $BiVO_4$, GCN, GCDs, and BCG-40.

View Article Online
DOI: 10.1039/D0NJ03375H

photoinduced carriers, usually, the smaller the radius of EIS Nyquist plots is, the higher the separation efficiency of charge carriers is. It can be seen from the Fig. 6b that the arc radius of BCG-40 was smaller than that of pure $BiVO_4$, GCN and GCDs, indicating that BCG-40 exhibited the highest photoactivity among those photocatalysts. And the above results are well consistent with the date of the PC and PL experiment.

3.1.7 BET analysis

BET surface area and Barrett-Joiner-Haled pore structure of the photocatalysts are investigated by nitrogen-adsorption isotherms. As shown in Fig. 7a, the adsorption-desorption curve of the catalysts belongs to the type IV isotherm, which corresponds to the mesoporous character of all investigated materials with a negligible amount of micropores. The specific surface areas of $BiVO_4$, GCN, GCDs and BCG-40 composite catalysts calculated by BET method were 2.7186 m^2/g, 23.7486 m^2/g, 24.1931 m^2/g, and 19.7876 m^2/g, respectively. It can be clearly observed that the addition of GCDs greatly increases the specific surface area of the $BiVO_4$. Although the specific surface area of the Z-scheme heterostructure photocatalyst is slightly lower than that of GCN, it cannot be ignored that the Z-scheme heterostructure can enhance the photocatalytic performance, and effective separation of photo-generated carriers is the dominating factor of photodegradation. From the pore size distribution in Fig. 7b, most of the pores were concentrated between 5-50 nm indicating the mesoporous structure, which is consistent with the characteristics of the IV isotherm. The bigger size of the photocatalyst pore structure will enhance the adsorption rate of the contaminant, and more detail date are summarized in Table 1.

Table 1

The BET specific surface area, pore volume and pore size of photocatalysts.

Sample	S_{BET} (m^2/g)	Pore Volume (cm^3/g)	Pore Diameter (nm)
$BiVO_4$	2.7186	0.0078	11.28
GCN	23.7486	0.1637	27.58
GCDs	24.1931	0.1564	25.85
BCG-40	19.7876	0.1026	20.78

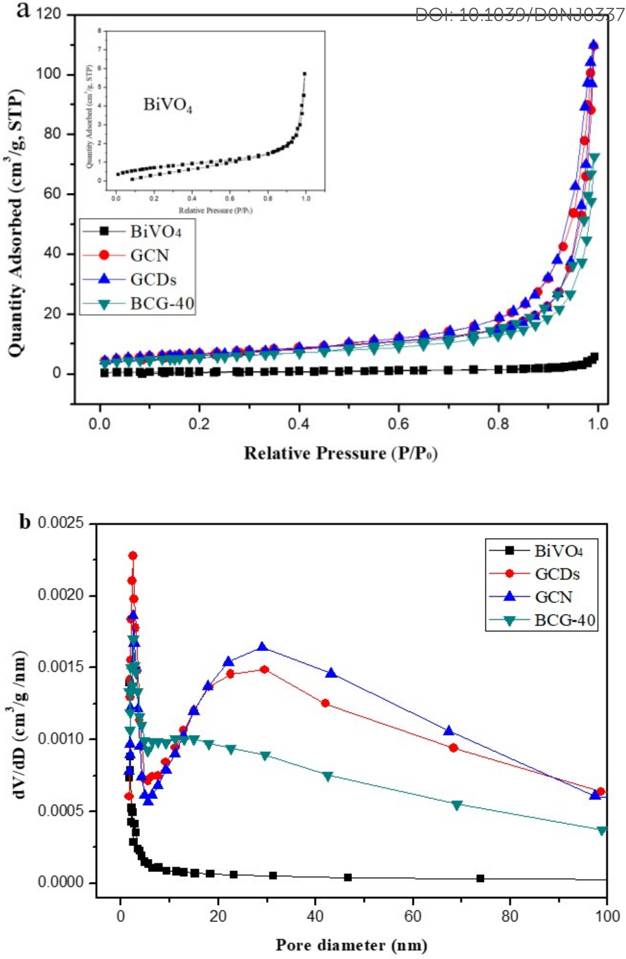

Fig. 7. (a) N_2 adsorption-desorption isotherms and (b) Barrett-Joiner-Helenda pore size distribution curves of the as-prepared photocatalysts.

3.2. Photocatalytic activity

Photodegradation efficiency of as-prepared photocatalysts was examined through the method described in *Section 2.5* above. And the specific situation of the concentration of RhB solution changing with the illumination time shown in Fig. 8a. Firstly, the concentration of RhB solution of the blank group has slight change, indicating that the photodecomposition of RhB solution itself was almost negligible. For pure $BiVO_4$ and GCN, the photocatalytic activity is also low, only 9.6 % and 60.48 % of RhB solution was degraded within 30 min. It is obvious that GCN/$BiVO_4$ can improve the photocatalytic efficiency, but the effect is still very limited. The BCG composite material obtained by introducing carbon dots can further inhibit the recombination of photogenerated carriers and enhance

View Article Online
DOI: 10.1039/D0NJ03375H

the photocatalytic activity, which is also consistent with PL spectroscopic analysis. Moreover, the research shows that the loading of $BiVO_4$ will affect the photocatalytic efficiency of BCG composites. When the proportion of $BiVO_4$ is 40%, the photocatalytic performance reaches the peak, and the degradation of RhB is the largest (85.1%), which is 1.4 and 8.8 times that GCN of and pure $BiVO_4$, respectively. And the more specific details are shown in Fig. S2.

The kinetic behavior of photocatalyst can been calculated as follows:

$$\ln\left(\frac{C_0}{C_t}\right) = kt, \tag{1}$$

where C_0 and C_t are the initial and final concentrations of targeted contaminants in the photocatalytic process, and k (min^{-1}) is the constant of equation [55]. As shown in the Fig. 8b, the k value of BCG-40 was 0.06317 min^{-1}, which is 18.7, 2.04, 1.87, 1.68, 1.54, 1.12 and 1.46 times higher than for $BiVO_4$, GCN, GCDs, GCN/$BiVO_4$, BCG-20, BCG-30 and BCG-50, respectively. This result further proves that the carbon dots coupling with $BiVO_4$ and GCDs can improve the photoactivity of the composite. And compared with previous reports, the degradation of RhB by BCG-40 photocatalyst under visible light was significantly improved in this work (as shown in Table 2).

Minocycline hydrochloride was used to simulate the degradation of antibiotic wastewater. As can be seen from Fig. 9a, under the same conditions, after 30 min of dark adsorption, the probability of self-degradation of minocycline hydrochloride under the light source is very low (16 %). However, after 140 min of light treatment, pure GCN, GCDs and pure $BiVO_4$ only degraded minocycline hydrochloride by 18 %, 22 % and 31 %, respectively. Unsurprisingly, the degradation rate of GCN/$BiVO_4$ is higher than that of GCN and $BiVO_4$ while much lower than that of BCG. The BCG-40 showed the highest photocatalytic degradation efficiency, and the removal rate of target pollutants reached 65.3% within 140 minutes. Combining the photodegradation process with a pseudo-first-order model and drawing a slope graph in Fig. 9b, the k value of BCG-40 is the largest, representing the best reaction rate in the process of photocatalysis. The above conclusions indicate that BCG-40 composite material also has great potential in removing antibiotics from wastewater.

Table 2

Comparison on the rates of photocatalytic degradation of RhB with different catalysts.

Catalyst	C (mg/L)	Time (min)	Degradation rate	Ref.
CN/$BiVO_4$	15	120	85 %	Jiang[56]
CDs/$BiVO_4$	10	120	95 %	Wang[57]
CN/SnO_2	10	150	93 %	Huang[58]
BiOCl/CN	10	80	96 %	Zhang[59]
BCG-40	20	30	85 %	This work

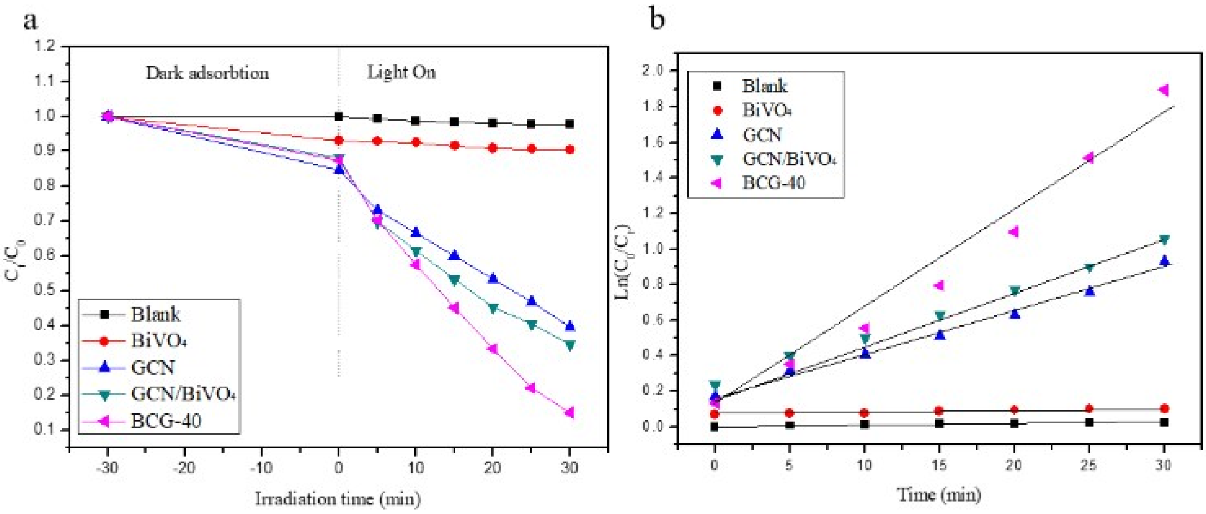

Fig. 8. (a) Photodegradation performance of as-prepared photocatalyst in removing RhB and (b) the kinetic behavior of RhB photodegradation over pure $BiVO_4$, GCN, GCN/$BiVO_4$ and BCG-40 composite.

View Article Online
DOI: 10.1039/D0NJ03375H

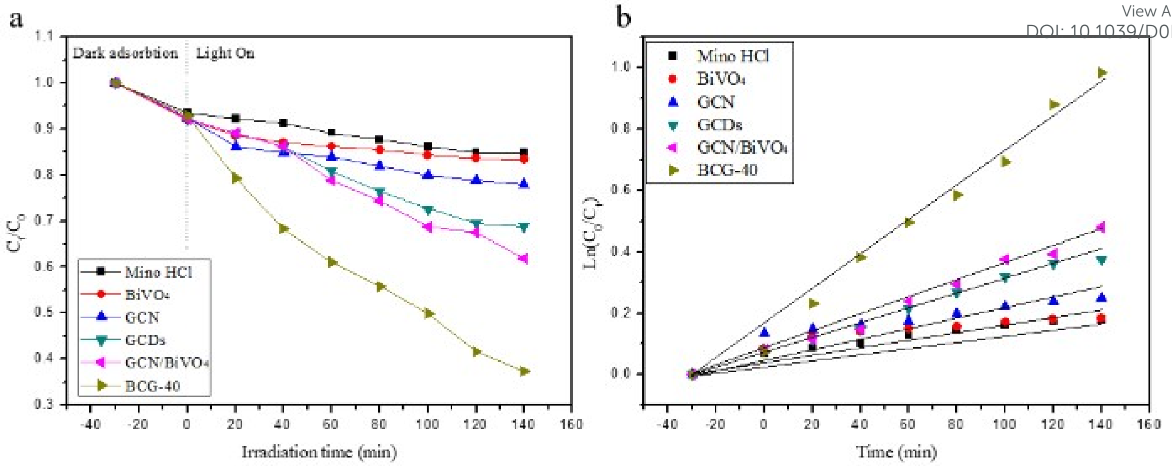

Fig. 9. (a) Photodegradation performance of as-prepared photocatalyst in removing Mino HCl and (b) the kinetic behavior of Mino-HCl photodegradation over pure GCN, $BiVO_4$, GCN, GCDs, GCN/$BiVO_4$ and BCG-40 composite.

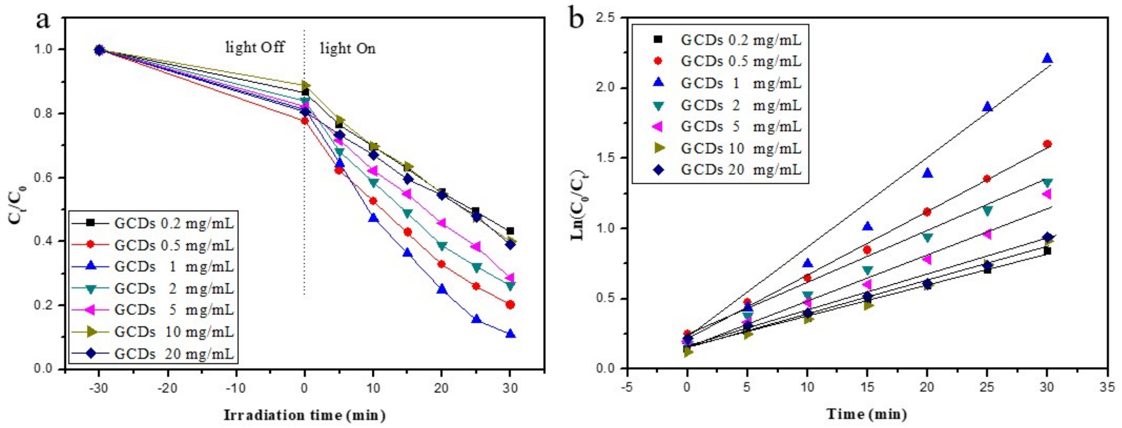

Fig. 10. Effect of different concentrations of C-Dots on the degradation of RhB.

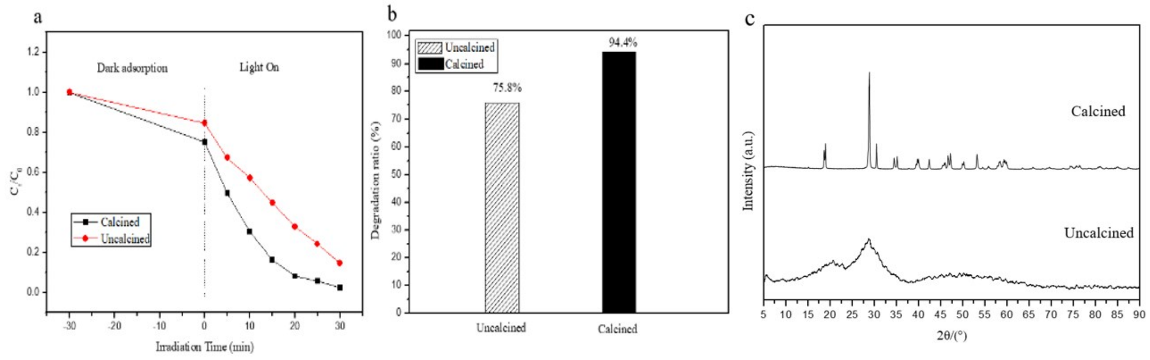

Fig. 11. (a-b) The degradation of RhB by BCG photocatalyst and (c) XRD patterns of $BiVO_4$ before and after calcination.

3.3 Effect of the doping amount of C-Dots

As we know, C-dots as the electron transfer center of Z-scheme heterojunction photocatalyst, can play a vital role in broadening the optical absorption region and decreasing electron-hole recombination events. In order to investigate the effect of the C-Dots doping amount on the photocatalytic activity of BCG, the concentration of C-Dots was gradually increased without changing the amount of $BiVO_4$ and GCN. From the Fig. 10, as the concentration of C-Dots increased from 0.2 mg/mL to 20 mg/mL, the photocatalytic degradation efficiency of the photocatalyst first increases and then decreases and reaches a peak at a concentration of 1 mg/mL. This indicates that an

View Article Online
DOI: 10.1039/D0NJ03375H

excessively large concentration of C-Dots will inhibit the photocatalytic performance. This phenomenon may be attributed to GCN itself can absorb visible light, and the high content of C-Dots forms a competitive relationship with GCN in the absorption of visible light, thereby reducing the efficiency of visible light degradation of RhB[60].

3.4 Effect of calcination on the synthesis of materials

As shown in Fig. 11a-b, the BCG-40 composite was calcined at 450 ℃ and used it for photocatalytic degradation of target pollutants (10 mg/mL RhB) under the same conditions. Obviously, the degradation rate of the photocatalyst after calcination was observed as high as 94.4%, the degradation rate of the catalyst without calcination is only 75.8%. It shows that the photocatalytic material after calcination shows more excellent photocatalytic performance. The reason for this phenomenon may be that the specific surface area of the composite material is increased by heat treatment, and the phases of the composite material are formed more closely, which creates better conditions for the electron transfer of the entire system, thereby promoting the system redox process. In addition, $BiVO_4$ has been proved to exist in three crystal forms, and the three crystal forms can be converted to each other at different temperatures[61]. When the temperature is maintained at 450 ℃, $BiVO_4$ is mainly composed of a monoclinic crystal form, and the ionic structure around this crystal form has a high degree of distortion and a very poor symmetry, which can greatly increase the degree of polarization and is conductive to electron-holes separation. As shown in Fig. 11c, the XRD pattern of $BiVO_4$ before and after calcination was determined. $BiVO_4$ prepared by hydrothermal method shows an amorphous structure, while the $BiVO_4$ after calcination has higher degree of monoclinic phase, narrower half peak width and greater peak intensity, and there is no other crystal phase diffraction peak. Therefore, this temperature-induced change in crystal form may also be one of the reasons for better photocatalytic activity after calcination.

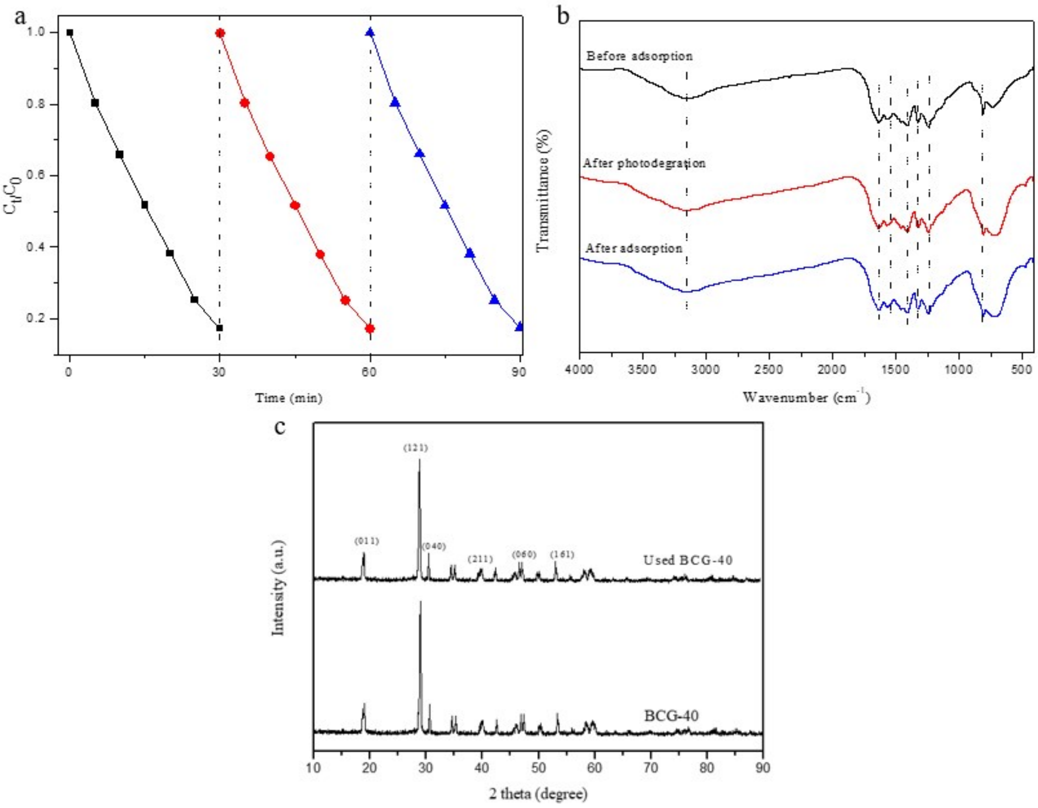

Fig. 12. (a) The recyclability tests of BCG composites under light irradiation before and after 3 recycles., and (b)FTIR, (c) XRD patterns of BCG composites before and after degradation.

View Article Online
DOI: 10.1039/D0NJ03375H

3.5 Photocatalytic recyclability and stability

Photocatalyst recycling and stability are important steps in evaluating environmentally friendly photocatalytic systems. Therefore, after centrifuging, washing and drying, the used photocatalyst was repeatedly tested under the same conditions to evaluate the stability of the BCG-40. As shown in Fig.12a, after 3 cycles of recycling, the degradation performance of BCG-40 photocatalyst is still stable, which indicated that the composite has a good chemical stability. The XRD and FTIR patterns of the BCG-40 before and after degradation have shown in Fig. 12b and Fig. 12c, respectively. No detectable changes were observed in the FTIR and XRD of the recovered and after adsorbed samples, indicating that the BCG composite has a small adsorption effect during the degradation, and has good photocatalytic activity and photostability.

3.6 Mechanism route analysis

In order to determine the active substances that appeared in the photodegradation of contaminants, we conducted a free radical trapping experiment. Fig.13a illustrated the degradation ratio of the contaminant after adding different scavengers, and EDTA-2Na, isopropanol (IPA), 4-benzoquinone (BQ) were used as scavengers of h^+_{VB}, ·OH and $\cdot O_2^-$, respectively. When a certain amount of h^+_{VB} scavenger (EDTA-2Na) is added, the removal rate of pollutants is only slightly changed compared to the system without scavenger, indicating that h_{VB} radical does not dominate the photocatalytic process. In the case of $\cdot O_2^-$ scavenger (BQ), the photocatalytic degradation performance was greatly inhibited, and the removal rate decreased from 89 % to 31 %, this result indicates that the $\cdot O_2^-$ radical played a vital role in the photodegradation of contaminants. However, the photocatalytic performance also decreased after the ·OH scavenger (IPA) was added, indicating that ·OH free radicals also participate in photocatalytic activities. Therefore, it can be judged that both $\cdot O_2^-$ free radicals and ·OH free radicals are the main active substances in photocatalytic degradation.

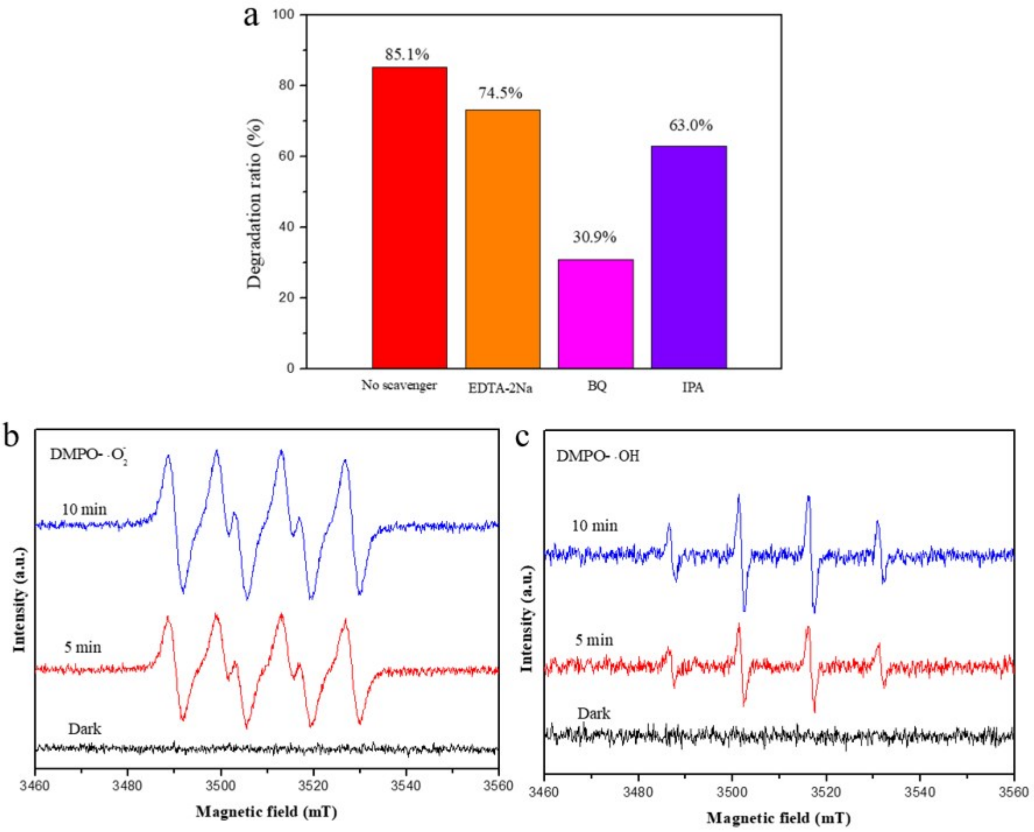

Fig. 13. (a) Trapping experiments of active species during the photocatalytic degradation. (b) DMPO spin-trapping ESR spectra for BCG-40 (b) in methanol (for DMPO- $\cdot O_2^-$) and (c) in aqueous dispersion (for DMPO- ·OH) under visible light irradiation.

View Article Online
DOI: 10.1039/D0NJ03375H

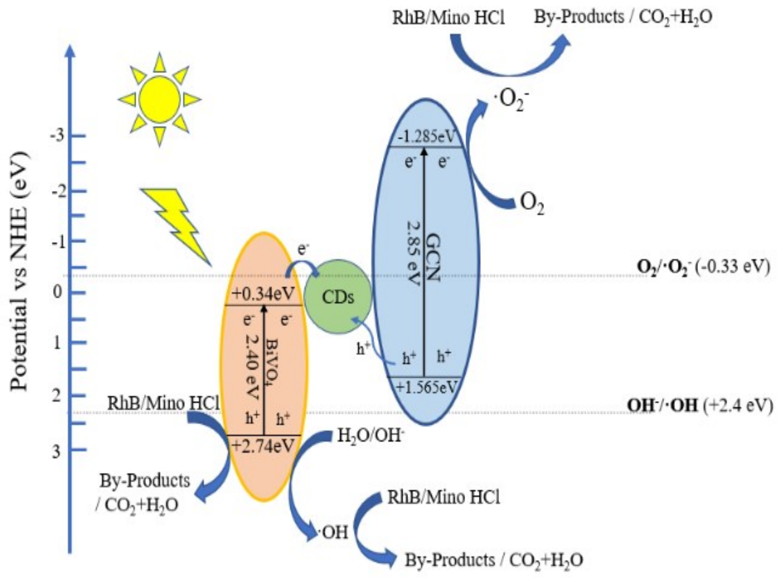

Fig. 14. The possible photocatalytic mechanism for the contamination.

To prove the Z-scheme mechanism and further confirm the main active species produced during this photodegradation system, ESR spectra were measured. As displayed in Fig. 13b and c, the typical peaks of DMPO- $\cdot O_2^-$ and DMPO- ·OH cannot be detected under dark conditions, while the obvious characteristic peaks of DMPO- $\cdot O_2^-$ and DMPO- ·OH species appeared under visible light irradiation. It is noteworthy that the signal intensity of DMPO- $\cdot O_2^-$ increases more than that of DMPO- ·OH from 5 to 10 min. Therefore, $\cdot O_2^-$ plays a more important role in the photodegradation process, which corresponds to that recorded in free radical trapping experiments.

As we all know, the band gap structure of the semiconductor affects the photocatalytic performance, which is related to the conduction band and valence band of the photocatalyst. The conduction band and valence band of the photocatalyst can be calculated by the following equations:

$$E_{CB}=X-E_c-E_g/2 \,, \qquad (2)$$

$$E_{VB}=E_{CB}+E_g \,, \qquad (3)$$

where X, E_{CB}, E_{VB} and E_g represent absolute electronegativity, conduction band potential and valence band potential and forbidden band width of the semiconductor, while Ec is the energy of the free electron on the hydrogen standard (about 4.5 eV). In general, the E_g of GCN and $BiVO_4$ are 2.85 eV and 2.40 eV, and X of GCN and $BiVO_4$ are 4.64 eV and 6.04 eV, respectively. Therefore, it can be calculated that the E_{CB} and E_{VB} of the GCN photocatalyst are −1.285 and 1.565 eV, while E_{CB} and E_{VB} of the $BiVO_4$ are 0.34 and 2.74 eV, respectively [35, 62, 63].

Combined with the free radical trapping experiments, Fig. 14 illustrate the possible mechanism of BCG-40 to photodegrade pollutants. Under the LED light irradiation, the generated photoelectrons and holes are allocated to their CB and VB, respectively. Moreover, C-Dots becomes the charge transmission bridge between GCN and $BiVO_4$. Therefore, the photoexcited electrons on the conduction band of $BiVO_4$ and the holes generated on the valence band of GCN are transferred to C-Dots, resulting in the electrons mainly concentrated on the conduction band of GCN, and the holes are mainly accumulated on the valence band of $BiVO_4$. This phenomenon improves the separation efficiency of photo-electrons and holes and inhibits its recombination, and showing the good photocatalytic performance of BCG. Moreover, the GCN has a more negative CB reduction potential than E° ($O_2/\cdot O_2^-$), and $BiVO_4$ has a more positive VB potential than E° (·OH /H_2O), then the photogenerated electrons generated by CB of GCN can be The O_2 reaction produces $\cdot O_2^-$, and holes can participate in the formation of ·OH. Therefore, in this Z-scheme

View Article Online
DOI: 10.1039/D0NJ03375H

heterojunction photocatalyst degradation process, $\cdot O_2^-$, $\cdot OH$ and h_{VB}^+ co-participate in the mineralization of RhB and minocycline hydrochloride, and finally achieve photocatalytic degradation.

$$BCG + h\nu \rightarrow BCG + e^- + h_{VB}^+ \quad (4)$$

$$e^- + O_2 \rightarrow \cdot O_2^- \quad (5)$$

$$\cdot O_2^- + H_2O \rightarrow \cdot OH + \cdot HO_2 \quad (6)$$

$$\cdot HO_2 + H_2O \rightarrow 3\cdot OH \quad (7)$$

$$h_{VB}^+ + OH^- \rightarrow \cdot OH \quad (8)$$

$$\cdot O_2^-/\cdot OH/h_{VB}^+ + \text{Pollutant} \rightarrow CO_2 + H_2O\ /\ \text{product} \quad (9)$$

4. Conclusion

In this work, a novel Z-scheme heterojunction $BiVO_4$/C-Dots/g-C_3N_4 composite photocatalyst was successfully synthesized by ultrasound, and the dye wastewater (RhB) and antibiotic wastewater (Mino-HCl) were degraded under LED light. In particularly, BCG-40 has the highest photocatalytic performance among BCG materials with different content ratios and after introducing of the C-dots, the photocatalytic activity of composites was enhanced than before. In addition, the free radical trapping experiments and ESR results have also proved the Z-scheme mechanism of this photocatalyst, and the C-dots serves as the carrier center of photogenerated carriers, which greatly expands the process of recombination of photogenerated carriers of the composite, and further improves the photocatalytic performance of BCG. Finally, photoexcited $\cdot O_2^-$, $\cdot OH$ and h_{VB}^+ have also been proved to be the primary and secondary active substance in the entire degradation and the repeatability test of recyclability also proved the good stability of the photocatalyst. This research is expected to contribute new ideas to the development of photocatalysts. Moreover, the effect of carbon dots with different luminescent properties on the photocatalytic performance of composite materials remains to be explored, we expect to complete it in subsequent researchers.

Conflicts of interest

There are no conflicts to declare.

Acknowledgment

This research did not receive any specific grant from funding agencies in the public, commercial, or not-for-profit sectors. Special thanks to eceshi (www.eceshi.cn) for the help of XPS and TEM analysis.

References

1. H. Wang, Y. Wu, M. B. Feng, W. G. Tu, T. Xiao, T. Xiong, H. X. Ang, X. Z. Yuan and J. W. Chew, *Water Research*, 2018, **144**, 215-225.
2. S. Y. Dong, L. F. Cui, W. Zhang, L. J. Xia, S. J. Zhou, C. K. Russell, M. H. Fan, J. L. Feng and J. H. Sun, *Chemical Engineering Journal*, 2020, **384**, 10.
3. W. H. Qian, J. J. Qiu and X. Y. Liu, *Journal of Periodontology*, 8.
4. F. Mashkoor and N. Abu, *Journal of Magnetism and Magnetic Materials*, 2020, **500**, 19.
5. D. Zhang, Y. Tang, X. Qiu, J. Yin, C. Su and X. Pu, *Journal of Alloys and Compounds*, 2020.
6. D. Kong, D. Yin, D. Zhang, F. Yuan and X. Pu, *Nanotechnology*, 2020.
7. D. Zhang, S. Liang, S. Yao, H. Li and X. Pu, *Sep Purif Technol*, 2020, **248**, 117040.
8. D. Zhang, C. Su, H. Li, X. Pu and Y. Geng, *Journal of Physics and Chemistry of Solids*, 2019, 109326.
9. S. Xu, P. Zhou, Z. H. Zhang, C. J. Yang, B. G. Zhang, K. J. Deng, S. Bottle and H. Y. Zhu, *Journal of the American Chemical Society*, 2017, **139**, 14775-14782.
10. X. B. Chen, L. Liu, P. Y. Yu and S. S. Mao, *Science*, 2011, **331**, 746-750.
11. M. Wang, C. Y. Jin, Z. L. Li, M. Y. You, Y. Zhang and T. Zhu, *Journal of Colloid and Interface Science*, 2019, **533**, 513-525.
12. M. Wang, P. Y. Guo, Y. Zhang, C. M. Lv, T. Y. Liu, T. Y. Chai, Y. H. Xie, Y. Z. Wang and T. Zhu, *Journal of Hazardous Materials*, 2018, **349**, 224-233.
13. Z. F. Jiang, W. M. Wan, H. M. Li, S. Q. Yuan, H. J. Zhao and P. K. Wong, *Advanced Materials*,

View Article Online
DOI: 10.1039/D0NJ03375H

2018, **30**, 9.

14. M. M. Zhang, C. Lai, B. S. Li, D. L. Huang, G. M. Zeng, P. Xu, L. Qin, S. Y. Liu, X. G. Liu, H. Yi, M. F. Li, C. C. Chu and Z. Chen, *Journal of Catalysis*, 2019, **369**, 469-481.
15. S. W. Cao, J. X. Low, J. G. Yu and M. Jaroniec, *Advanced Materials*, 2015, **27**, 2150-2176.
16. Y. Wang, X. Wang and M. Antonietti, *Angewandte Chemie-International Edition*, 2012, **51**, 68-89.
17. M. J. Lima, A. M. T. Silva, C. G. Silva and J. L. Faria, *Journal of Catalysis*, 2017, **353**, 44-53.
18. E. J. Son, S. H. Lee, S. K. Kuk, M. Pesic, D. S. Choi, J. W. Ko, K. Kim, F. Hollmann and C. B. Park, *Advanced Functional Materials*, 2018, **28**, 9.
19. F. H. Li, R. R. Zhao, B. Y. Yang, W. Wang, Y. Liu, J. P. Gao and Y. L. Gong, *International Journal of Hydrogen Energy*, 2019, **44**, 30185-30195.
20. K. Prakash, J. V. Kumar, P. Latha, P. S. Kumar and S. Karuthapandian, *Journal of Photochemistry and Photobiology a-Chemistry*, 2019, **370**, 94-104.
21. B. Liu, L. Q. Ye, R. Wang, J. F. Yang, Y. X. Zhang, R. Guan, L. H. Tian and X. B. Chen, *Acs Applied Materials & Interfaces*, 2018, **10**, 4001-4009.
22. Y. Deng, L. Tang, C. Feng, G. Zeng, J. Wang, Y. Lu, Y. Liu, J. Yu, S. Chen and Y. Zhou, *Acs Applied Materials & Interfaces*, 2017, **9**, 42816-42828.
23. X. Miao, D. Qu, D. X. Yang, B. Nie, Y. K. Zhao, H. Y. Fan and Z. C. Sun, *Advanced Materials*, 2018, **30**, 8.
24. G. L. Wu, Y. H. Cheng, Z. H. Yang, Z. R. Jia, H. J. Wu, L. J. Yang, H. L. Li, P. Z. Guo and H. L. Lv, *Chemical Engineering Journal*, 2018, **333**, 519-528.
25. M. Han, S. Zhu, S. Lu, Y. Song, T. Feng, S. Tao, J. Liu and B. Yang, *Nano Today*, 2018, **19**, 201-218.
26. M. Han, S. J. Zhu, S. Y. Lu, Y. B. Song, T. L. Feng, S. Y. Tao, J. J. Liu and B. Yang, *Nano Today*, 2018, **19**, 201-218.
27. X. Y. Wang, M. Y. Lu, J. Ma, P. Ning and L. Che, *Journal of the Taiwan Institute of Chemical Engineers*, 2018, **91**, 609-622.
28. F. Q. Zhou, J. C. Fan, Q. J. Xu and Y. L. Min, *Applied Catalysis B Environmental*, 2017, **201**, 77-83.
29. M. L. Guan, D. K. Ma, S. W. Hu, Y. J. Chen and S. M. Huang, *Inorganic Chemistry*, 2011, **50**, 800-805.
30. J. Q. Yu, Y. Zhang and A. Kudo, *Journal of Solid State Chemistry*, 2009, **182**, 223-228.
31. Zizai, Ma, Kai, Song, Lin, Wang, Fengmei, Gao, Bin and Tang.
32. S. Wei, X. Yin, H. Li, X. Du, L. Zhang, Q. Yang and R. Yang, *Chemistry (Weinheim an der Bergstrasse, Germany)*, 2020.
33. Q. Liu, T. Chen, Y. Guo, Z. Zhang and X. Fang, *Applied Catalysis B Environmental*, **193**, 248-258.
34. X. Rong, F. Qiu, J. Rong, X. Zhu, J. Yan and D. Yang, *Materials Letters*, 2016, **164**, 127-131.
35. Q. G. Meng, H. Q. Lv, M. Z. Yuan, Z. Chen, Z. H. Chen and X. Wang, *Acs Omega*, 2017, **2**, 2728-2739.
36. R. Z. Sun, Q. M. Shi, M. Zhang, L. H. Xie, J. S. Chen, X. M. Yang, M. X. Chen and W. R. Zhao, *Journal of Alloys and Compounds*, 2017, **714**, 619-626.
37. Z. Q. He, Y. Q. Shi, C. Gao, L. N. Wen, J. M. Chen and S. Song, *Journal of Physical Chemistry C*, 2014, **118**, 389-398.
38. R. L. Frost, D. A. Henry, M. L. Weier and W. Martens, *Journal of Raman Spectroscopy*, 2006, **37**, 722-732.
39. S. K. Lakhera, H. Y. Hafeez, R. Venkataramana, P. Veluswamy, H. Choi and B. Neppolian, *Applied Surface Science*, 2019, **487**, 1289-1300.
40. X. P. Dong and F. X. Cheng, *Journal of Materials Chemistry A*, 2015, **3**, 23642-23652.
41. K. R. Reddy, C. V. Reddy, M. N. Nadagouda, N. P. Shetti, S. Jaesool and T. M. Aminabhavi, *Journal of Environmental Management*, 2019, **238**, 25-40.

42. J. Q. Yu and A. Kudo, *Advanced Functional Materials*, 2006, **16**, 2163-2169.
43. Y. Wang, G. Q. Tan, T. Liu, Y. N. Su, H. J. Ren, X. L. Zhang, A. Xia, L. Lv and Y. Liu, *Applied Catalysis B-Environmental*, 2018, **234**, 37-49.
44. H. Y. Hafeez, S. K. Lakhera, S. Bellamkonda, G. R. Rao, M. V. Shankar, D. W. Bahnemann and B. Neppolian, *International Journal of Hydrogen Energy*, 2018, **43**, 3892-3904.
45. Y. Cheng, R. Q. Song, K. Wu, N. Peng, M. Yang, J. Luo, T. Zou, Y. G. Zuo and Y. Liu, *Journal of Hazardous Materials*, 2020, **383**, 10.
46. Y. C. Deng, L. Tang, C. Y. Feng, G. M. Zeng, Z. M. Chen, J. J. Wang, H. P. Feng, B. Peng, Y. N. Liu and Y. Y. Zhou, *Applied Catalysis B-Environmental*, 2018, **235**, 225-237.
47. Y. Gong, H. K. Li, C. Jiao, Q. C. Xu, X. Y. Xu, X. M. Zhang, Y. F. Liu, Z. Y. Dai, X. Y. Liu, W. Chen, L. Liu and D. Zhan, *Applied Catalysis B-Environmental*, 2019, **250**, 63-70.
48. Z. Y. Fang, Y. Z. Hong, D. Li, B. F. Luo, B. D. Mao and W. D. Shi, *Acs Applied Materials & Interfaces*, 2018, **10**, 20521-20529.
49. L. Q. Ye, J. Y. Liu, Z. Jiang, T. Y. Peng and L. Zan, *Applied Catalysis B-Environmental*, 2013, **142**, 1-7.
50. Q. G. Pan, K. R. Yang, G. L. Wang, D. D. Li, J. Sun, B. Yang, Z. Q. Zou, W. B. Hu, K. Wen and H. Yang, *Chemical Engineering Journal*, 2019, **372**, 399-407.
51. L. D. Jiang, D. Chen, L. S. Qin, J. H. Liang, X. G. Sun and Y. X. Huang, *Journal of Alloys and Compounds*, 2019, **783**, 10-18.
52. Y. Liu, G. Zhu, J. Gao, M. Hojamberdiev, R. Zhu, X. Wei, Q. Guo and P. Liu, *Applied Catalysis B-Environmental*, 2017, **200**, 72-82.
53. Y. Z. Li, X. J. Wang and L. Z. Gao, *Journal of Materials Science-Materials in Electronics*, 2019, **30**, 16015-16029.
54. D. Z. A, C. S. A, S. Y. A, H. L. A, X. P. A and Y. G. B, *Journal of Physics and Chemistry of Solids*, 2020.
55. Y. Y. Zhao, Y. B. Wang, X. H. Liang, H. X. Shi, C. J. Wang, J. Fan, X. Y. Hu and E. Z. Liu, *Applied Catalysis B-Environmental*, 2019, **247**, 57-69.
56. T. Q. Jiang, F. Nan, J. Zhou, F. G. Zheng, Y. Y. Weng, T. Y. Cai, S. Ju, B. Xu and L. Fang, *Aip Advances*, 2019, **9**, 7.
57. Y. Wang, L. P. Sun, L. Chudal, N. K. Pandey, M. B. Zhang and W. Chen, *Chemistryselect*, 2019, **4**, 14103-14110.
58. Q. Y. Huang, Q. Zhao, C. Yang and T. S. Jiang, *Reaction Kinetics Mechanisms and Catalysis*, 2020, **129**, 535-550.
59. X. Zhang, D. An, D. Feng, F. Liang, Z. Chen, W. Liu, Z. Yang and M. Xian, *Applied Surface Science*, 2019, **476**, 706-715.
60. X. Yu, J. Liu, Y. Yu, S. Zuo and B. Li, *Carbon*, 2014, **68**, 718-724.
61. A. Kudo, K. Omori and H. Kato, 2010, **31**, no-no.
62. K. F. Zhang, Y. X. Liu, J. G. Deng, S. H. Xie, H. X. Lin, X. T. Zhao, J. Yang, Z. Han and H. X. Dai, *Applied Catalysis B-Environmental*, 2017, **202**, 569-579.
63. M. F. R. Samsudin, N. Bacho, S. Sufian and Y. H. Ng, *Journal of Molecular Liquids*, 2019, **277**, 977-988.

View Article Online
DOI: 10.1039/D0NJ03375H

Abstract graphic

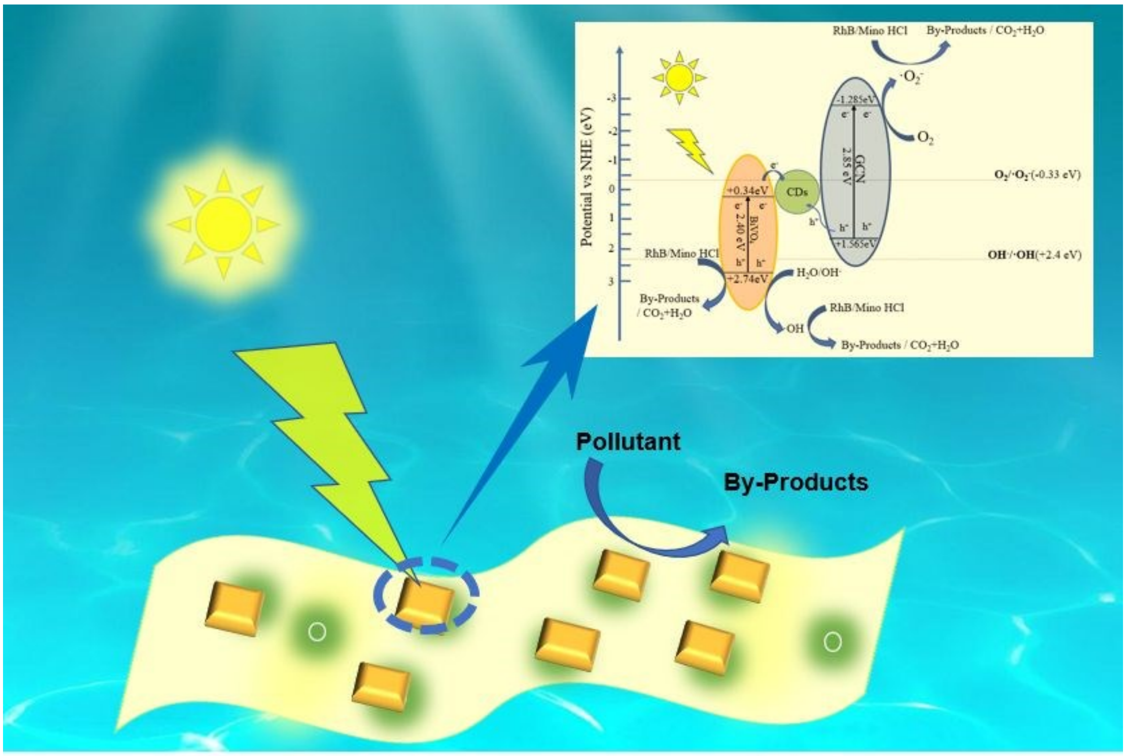

This research was highlighted as follows:

- $BiVO_4$/C-Dots/g-C_3N_4 Z-scheme photocatalyst with C-Dots as effective electrons transfer center were designed.
- Minocycline hydrochloride was effectively degraded by BCG-40 composites under LED irradiation
- C-Dots broaden visible light harvesting and inhibit the recombination of photoelectrons and holes.
- The optimization of photocatalytic performance was investigated by changing synthesis conditions and ratio